# รายงานฉบับสมบูรณ์

ทุนอุดหนุนวิจัย ประจำปี 2558

ชื่อโครงการ:

## การฝังอนุภาคนาโนซิลิกอนลงในวัสดุที่มีค่าคงคัวไดอิเล็กทริกสูง
## Integration of Silicon nanoparticles in high-k materials

รหัสโครงการวิจัย **ว-ท(ด)107.58**

หัวหน้าโครงการ:

ดร. จรรยา เจตนาเสน
ภาควิชาเคมี คณะวิทยาศาสตร์ ม.เกษตรศาสตร์

# Final Report

**Project Title** Integration of Silicon nanoparticles in high-k materials

**By** Dr. Junya Jettanasen

# Abstract

---

Silicon nanoparticles (Si-NPs) obtained by electrochemical etching of silicon wafer were incorporated into dielectric materials using Sol-Gel method. To attain a wide range of dielectric constant and band gap energy, three matrices are selected ($SiO_2$, $ZrO_2$ and $TiO_2$) and the Si-NPs were incorporated in these matrices in the form of powder and thin films. Structural studies by Transmission Electron Microscopy and Raman spectroscopy confirm the presence of Si-NPs in the matrices. Photoluminescence studies show that Si-NPs preserve their luminescent properties in $SiO_2$ matrix and $ZrO_2$ matrix but not in $TiO_2$ matrix. The PL peak position depends not only on the dimension of Si-NPs but also depends on their concentrations. This is due to the coupling effect between the nanoparticles which increases with concentration. The effect of annealing temperature is also studied for nanoparticles incorporated in thin films.

**Keywords :** high-K dielectric materials, silicon nanoparticles, porous silicon, sol-gel

# บทคัดย่อ

อนุภาคนาโนซิลิกอนที่ได้มาจากการกัดกร่อนทางไฟฟ้าเคมีถูกเติมลงในวัสดุ ไดเล็กทริกด้วยวิธีการทางโซล-เจล เพื่อที่จะได้ย่านของค่าคงตัวไดอิเล็กทริกและ band gap ค่อนข้างกว้าง แมทริกซ์สามชนิดได้ถูกเลือก ($SiO_2$, $ZrO_2$ and $TiO_2$) และอนุภาคนาโนซิลิกอนถูกฝังลงในแมทริกซ์เหล่านี้ในรูปแบบของผงละเอียดและ แบบฟิล์มบาง การศึกษาโครงสร้างด้วยกล้องจุลทรรศน์อิเล็กตรอนแบบส่องผ่านและ และรามานสเปกโทรสโกปียืนยันการมีอยู่ของอนุภาคนาโนซิลิกอนในแมทริกซ์ การศึกษาการเรืองแสงแสดงให้เห็นว่า อนุภาคนาโนซิลิกอนรักษาคุณสมบัติการเรืองแสงไว้ได้เมื่ออยู่ในแมทริกซ์ $SiO_2$ และ $ZrO_2$ แต่ไม่เรืองแสงใน $TiO_2$ ตำแหน่งของพีคการเรืองแสง ไม่ได้ขึ้นอยู่กับขนาด เพียงอย่างเดียว แต่ขึ้นอยู่กับความเข้มข้นของอนุภาคด้วย เนื่องจากการเกิดปรากฏการณ์ coupling ระหว่างอนุภาคที่อยู่ใกล้เคียงกัน จะเพิ่มขึ้นเมื่อความเข้มข้นเพิ่ม อิทธิพลของอุณหภูมิได้ถูกศึกษาด้วยเช่นกันสำหรับอนุภาคนาโนซิลิกอนที่ฝังอยู่ในฟิล์มบาง

**คำหลัก :** วัสดุค่าคงตัวไดเล็กทริกสูง, อนุภาคนาโนซิลิกอน, ซิลิกอนรูพรุน, โซล-เจล

# Acknowledgements

---

We would like to thank Kasetsart University Research and Development Institute (KURDI) for financial support, and the Department of Chemistry, Faculty of Science, Kasetsart University for all research facilities.

Also, we wish to thank Dr. Olivier Marty and Dr.Vladimir Lysenko at Institut des Nanotechnologies de Lyon (INL), UMR-5270 CNRS-UCBL-INSA-ECL, Université Claude Bernard-Lyon 1 for their help in experimental measurements and useful discussion.

# TABLE OF CONTENTS

# Introduction

---

Silicon based nano-device is one of the most motivating issues in nanotechnology development for more than decade [1]. In many applications such as nanomemory capacitors, single electron transistors, photodetectors, fiber optics and light-emitting devices, silicon nanoparticles (Si-NPs) are often embedded in silica matrix and various techniques have been applied to synthesize silicon nanostructures inside silica matrix [2-5].

Recently, the miniaturization trend in nanoelectronics has required replacing of silica matrix by other oxides having higher dielectric constants (high-k); for examples, $ZrO_2$, $HfO_2$, $Al_2O_3$, $Y_2O_3$, $La_2O_3$, and etc. [6, 7]. Therefore, for monolithic integration in future electronic devices, it is interesting to understand the influence of different dielectric matrices on the Si-NPs properties. In this work, three types of oxides were selected ($SiO_2$, $ZrO_2$, $TiO_2$) and the NPs were incorporated into the matrix by Sol-Gel technique. In fact, the Sol-Gel technique is promising because it offers many advantages such as high purity, relatively low processing temperature, large working area, inexpensive facilities, low operation costs and diversity of oxides obtained [8-11].

In general, to fabricate silicon nanoparticles, various methods can be employed, for example laser pyrolysis, aerosols, plasma deposition, electrochemical etching of silicon wafers, and etc [1]. In this work, we have chosen the electrochemical etching technique because of some drawbacks of the others techniques such as complexity of the process and high fabrication cost. The porous layers obtained after electrochemical etching will be finally milled into fine powders and incorporated into the matrices at different concentrations. All samples will be then characterized by Raman scattering, PL spectroscopy and Transmission electron microscopy. The impact of host matrices on the Si-NPs properties will be investigated, especially, stress induced structural modification of the NPs, photoluminescence, conditions for quantum confinement of photogenerated charge carriers in the Si-NPs localized in different matrices, and oxidation of the Si-NPs occurred inside the matrix.

## Objectives

1. To incorporate silicon nanoparticles obtained by electrochemical etching in different dielectric materials, especially, high-K dielectrics.
2. To study the properties of silicon nanoparticles encapsulated in different matrices obtained by Sol-Gel technique.
3. To confirm the feasibility to apply the Sol-Gel technique to the fabrication of nanoelectronic devices.

# Literature Reviews

---

## 1. Silicon nanoparticles fabrication

Several procedures have been developed throughout the last decade for the synthesis of luminescent Si nanoparticles [1]. These include physical, physiochemical, chemical, and electrochemical procedures. We will discuss briefly the procedures, size, uniformity in size, throughput, cost, and amenability to mass production, and recovery.

### *1.1 Physical Techniques*

Many physical techniques were developed in the last decade. First, Si nanoclusters were formed, for example, in the matrices of glass and $SiO_2$. In these efforts, luminescent nanocrystals of ~3 nm across embedded in quartz by implanting high-energy Si ions into quartz, followed by annealing at 1100°C were created. Second, silicon wafers were dispersed by ablation using a variety of agents to produce isolated Si particles. These agents included spark and laser ablation. In laser ablation, a focused high-power laser radiation is used as a brute force to blast the wafer. The broken pieces are transported downstream from the laser/material target by an inert gas jet, to be collected by filters. The particles are then recovered from the filter. These ablation techniques suffer from low throughput and cost, lack of control on the size and quality of the particles produced.

### *1.2 Physico-Chemical Techniques*

Isolated particles were obtained by the gas-phase preparation from silanes via slow combustion, thermal decomposition, microwave plasma, gas-evaporation, or chemical vapor deposition (CVD). Such methods may involve particle formation in a discharge of gas mixtures that include the highly toxic silane ($SiH_4$), followed by collection in filters and recovery from filters. These techniques suffer from low throughput and cost, lack of control on the size and shape of the particles. Although the decomposition of silanes produces nanoparticles with a relatively small size distribution, it does not lend itself to the easy manipulation of the surface of the particles, covered with $SiO_2$, or to their large-scale manufacturing.

### *1.3 Chemical Techniques*

Recently Si nanoclusters in the range 2–10 nm were synthesized chemically via a reduction of anhydrous ionic salts $SiX_4$ (X = Cl, Br), dispersed in water-free reverse-micelles solutions, with $LiAlH_4$. A certain degree of control over the Si cluster size was achieved by variation of the micelles size, intermicellar interaction, and reaction chemistry. Unlike the physical preparations, which produce impure Si crystallites that contain a large amount of $SiO_2$ on the surface, this method produces Si particles with the surface terminated by hydrogen from metal hydride. However, the formed Si particles are stable for long time (6 months to 1 year) only in a glove box under Ar. They would undergo degradation upon exposure to oxygen, presumably due to surface oxidation. Finally, organic capping of nanoparticles has been used as a means to achieve some degree of control over the particle size, directly during the synthesis step. This has been achieved in solution synthesis procedures using molecular silicon compounds. Methods of chemical reduction of Si (IV) compounds such as $SiR_nCl_{4-n}$ (R = H, alkyl) to Si (0) have been shown to directly produce organic-monolayerstabilized Si particles.

### 1.4 Electrochemical Techniques

Electrochemical dissolution of silicon followed by a means to separate particles, such as ultrasonic fracturing or milling of porous layers with high porosity, produces colloidal suspension of particles in a variety of organic solvents. The porous layer (formed under electrochemical anodization of crystalline Si wafers in HF-containing electrolysis bath) has a highly complex nanoscale architecture. It is to be noted that these layers are hydride terminated (containing very little $SiO_2$), with mono- ($\equiv SiH$), di- ($=SiH_2$) and tri- ($-SiH_3$) hydride groups in a variety of different local orientations and environments, owing to the complex porous nature of the material. Ultrasonic dispersion of electrochemically etched Si wafers in a variety of solvents results in a colloidal suspension of Si particles. The size distribution depends on the anodization time and the composition of the electrolysis bath solution. Unlike the gas-phase preparation of colloidal particles, this technique is more convenient and starts from high-purity semiconductor-grade substrates. More importantly, the resulting H-passivation of the surface minimizes its contamination by $SiO_2$ and other impurities.

## 2. Porous silicon

Porous silicon (PS) is the focus of intensive research for more than a decade due to its extremely promising properties such as increase in surface to volume ratio, quantam confinement, direct bandgap, photoluminesecence at room temperature, and etc. These specific properties contribute to the researchers interested in porous silicon applications.

### 2.1 Fabrication of porous silicon

Porous silicon is formed by electrochemical anodization (electrochemical etching) [12]. This method shows highly potential owing to low cost, simplicity of fabrication, and large quantity of nanoparticles obtained. By controlling etching time, concentration of electrolyte (HF), current density, wafer type (doping) and resistivity, the porous silicon layers can be prepared.

### *2.2 Electrolyte*

Hydrofluoric (HF) solution is used as electrolyte and absolute ethanol is usually added to the aqueous solution to increase the wettability of the surface due to its hydrophobic characteristics and to decrease the viscosity of the solution. In fact, ethanol penetrates the pores while purely aqueous HF solutions do not. This is very important for the lateral homogeneity and the uniformity of the PS layer in depth. In addition, during the reaction, hydrogen gas is produced. In pure aqueous solutions, bubbles are formed and stick on the silicon surface whereas they are promptly removed if ethanol (or some other surfactant) is present.

### *2.3 Anodization cell*

For electrochemical anodization of porous silicon, 3 types of anodization cell are utilized.

#### *a) Lateral anodization cell*

Lateral anodization cell is the simplest electrochemical cell. The cell body is a beaker made of highly resistant polymer such as Teflon. The silicon wafer works as the anode and the platinum or the other HF-resistant and conductive material acts as the cathode. The Si wafer is exposed to HF to form porous silicon between the point A and point B as shown in Figure 1. Lateral position of the wafer leads to different values of local current density and causes the inhomogeneity in porosity and thickness of the porous layers.

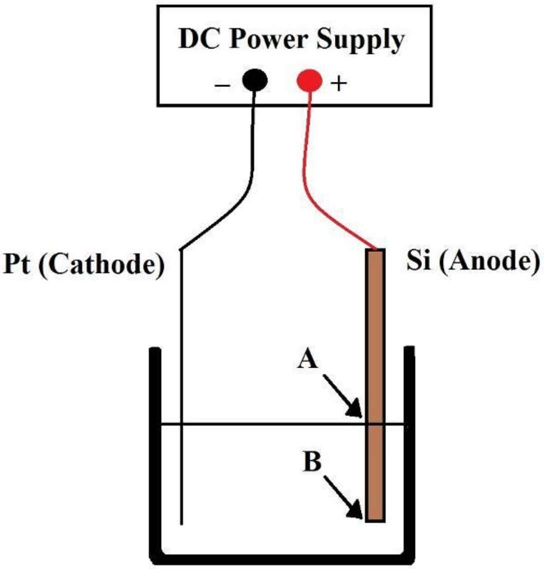

**Figure 1** Lateral anodization cell

*b) Single tank anodization cell*

For single tank anodization cell, the platinum wire works as the cathode and the anode is a copper plate. In this case, the silicon wafer is placed on the copper plate and sealed through an O-ring, so that only the front side of the sample is exposed to the electrolyte. Moreover, to promote hydrogen bubble removal and to avoid the decrease in local concentration of HF, overhead stirrer is utilized.

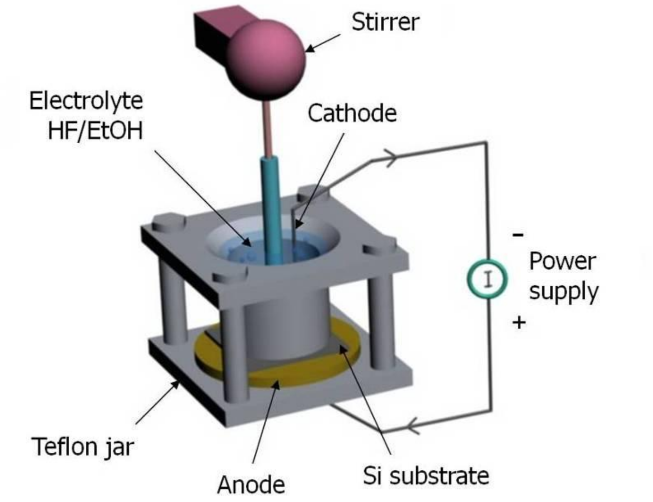

**Figure 2** Single tank anodization cell

*c) Double tank anodization cell*

The last type of anodization cell has a double tank geometry which has an electrolytic solution at the backside of silicon wafer. This cell composes of two half-cells in which platinum electrodes are immersed. The silicon wafer is placed between the two half-cells. A better uniformity is obtained using spiral or large Pt plates as the cathode and the anode. The current flows from cathode to anode through the Si wafer. In fact, the backside of the silicon wafer acts as a secondary cathode, while the front side of the wafer acts as a secondary anode where PS is formed. For this type of anodization cell, most of the problems encountered with the solid back contact in highly resistive samples are greatly reduced. For the same reason as the other cell, HF solution is circulated by overhead stirrer to remove the gas bubbles and control the stability of HF concentration.

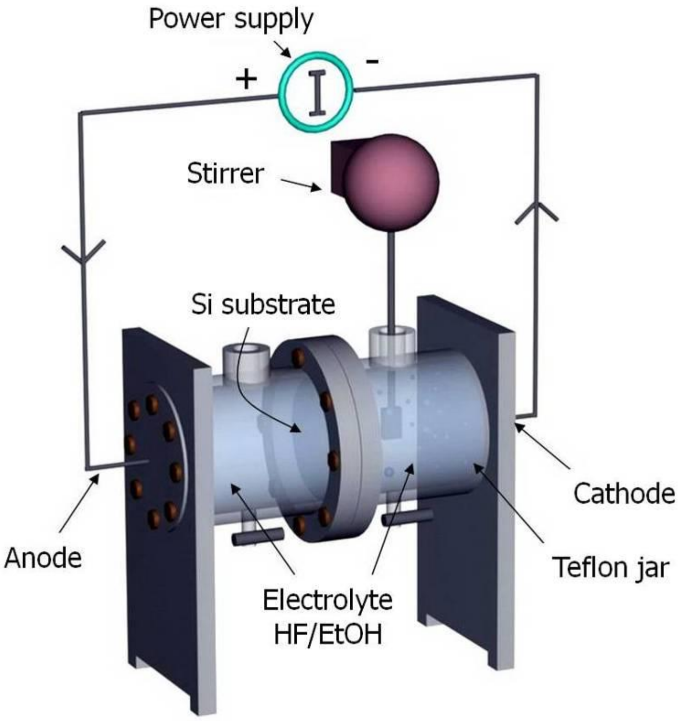

**Figure 3** Double tank anodization cell

*2.2 Dissolution mechanism*

Although the complete understanding of the silicon dissolution mechanism is still under study, the mostly accepted theory describes that holes are required for pore formation. During the anodization process, the positively charged silicon surface is oxidized by fluoride ions followed by the formation of water-soluble $H_2SiF_6$ complex as shown in Figure 4.

| | |
|---|---|
| 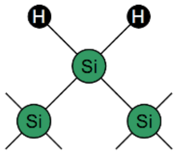 | In the absence of electron holes, a hydrogen saturated silicon surface is virtually free from attack by fluoride ions in the HF based electrolyte. The induced polarization between the hydrogen and silicon atoms is low because the electron affinity of hydrogen is similar to that of silicon. |
| 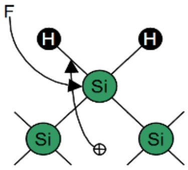 | If a hole reaches the surface, nucleophillic attack on a Si-H bond by a fluoride ion can occur and a Si-F bond is formed. |
| 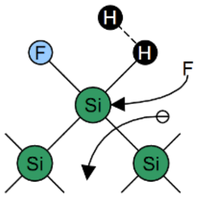 | The Si-F bond causes a polarization effect allowing a second fluorine ion to attack and replace the remaining hydrogen bond. Two hydrogen atoms can then combine, injecting an electron into the substrate. |
| 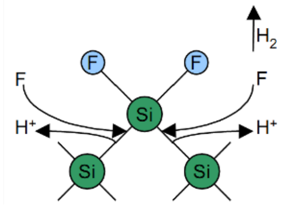 | The polarization induced by the Si-F bonds reduces the electron density of the remaining Si-Si backbonds making them susceptible to be attacked by the HF. Finally, the remaining silicon surface atoms are bonded to the hydrogen atoms. |
| 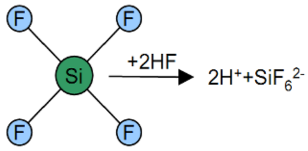 | The silicon tetrafluoride molecule reacts with the HF to form the highly stable $SiF_6^{-}$. |
| 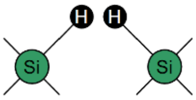 | The surface returns to its “neutral” state until another hole is made available. |

**Figure 4** Dissolution mechanism during pore formation [13]

After the dissolution of silicon, 3 different regions are found: (see Figure 5) In Region **A**, pore formation occurs, but in Region **C**, silicon is electropolished. Region **B** is a transition zone between Regions **A** and **C**. Note that scale units and zeros are arbitrarily chosen and depend on silicon sample and experimental conditions.

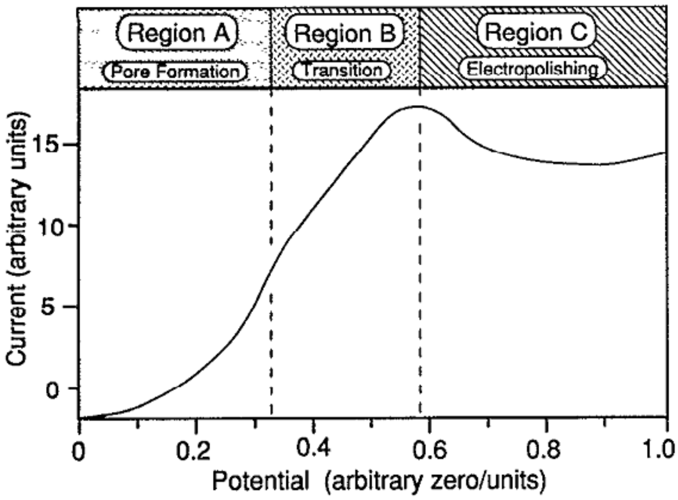

**Figure 5** Typical anodic I-V relationship for silicon in HF showing the 3 regions of dissolution [14].

These 3 different regions can also be presented as a function of current density and HF concentration as depicted in Figure 6. It demonstrates that porous silicon formation is favored at high HF concentrations and low current densities, while electropolishing is favored at low HF concentrations and high current densities.

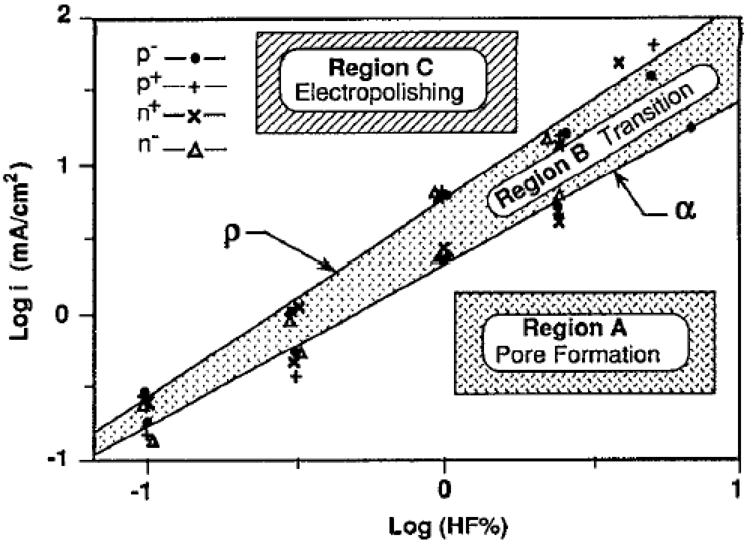

**Figure 6** The different regions of silicon dissolution as a function of current density and HF concentration [14].

### *2.4 Pore formation*

No complete understanding of the pore formation mechanisms exists because of the large number of parameters involved. Nevertheless, some models were proposed in order to explain the pore formation mechanisms, for example, fractal-like model. Figure 7 shows the fractal-like model (geometrical model) of porous silicon structure proposed by Wesolowski [15]. This model is in good agreement with the experimental results (see Figure 8). In fact, the most dominant structure occurs when the primary pore, which is perpendicular to the surface, has some microns of length and generates a second generation of smaller pores, which generates the next one, and etc. Smaller pores are rather perpendicular to the previous pores.

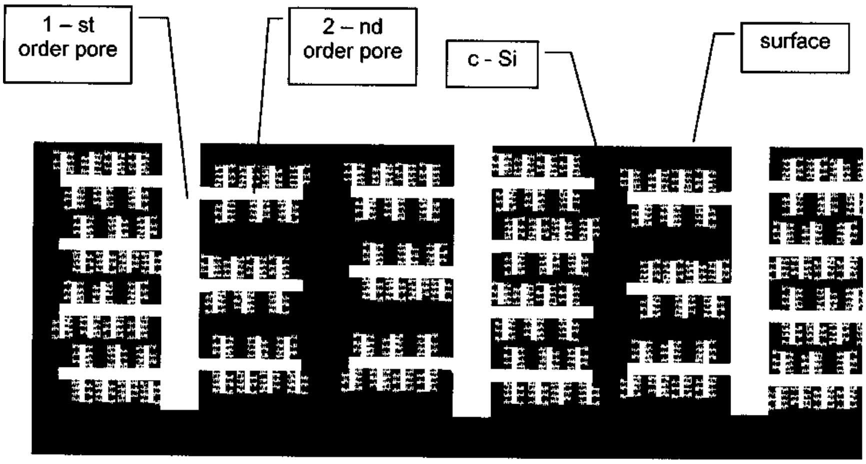

**Figure 7** Porous silicon structure network proposed by Wesolowski [15].

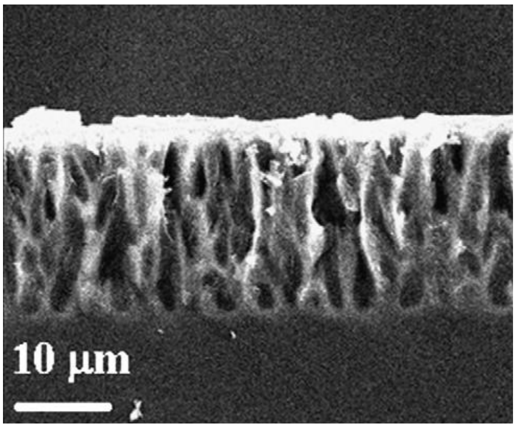

**Figure 8** Sponge-like structure of PS observed by SEM [16].

### *2.5 Influence of anodization conditions*

The properties of porous silicon, such as porosity, thickness, pore diameter and microstructure, depend on anodization conditions. These conditions include HF concentration, current density, wafer type and resistivity, anodization duration, illumination (n-type mainly), temperature, ambient humidity and drying conditions (see Table 1).

**Table 1** Effect of anodization conditions on porous silicon formation

| An increase of ... yields a | Porosity | Etching rate | Critical current |
|---|---|---|---|
| HF concentration | Decrease | Decrease | Increase |
| Current density | Increase | Increase | - |
| Anodization time | Increase | Almost constant | - |
| Temperature | - | - | Increase |
| Wafer doping (p-type) | Decrease | Increase | Increase |
| Wafer doping (n-type) | Increase | Increase | - |

### *2.6 Luminescence of porous silicon*

To understand the luminescence of porous silicon, many explanations have been proposed and can be grouped in 6 different categories, as illustrated in the scheme in Figure 9.

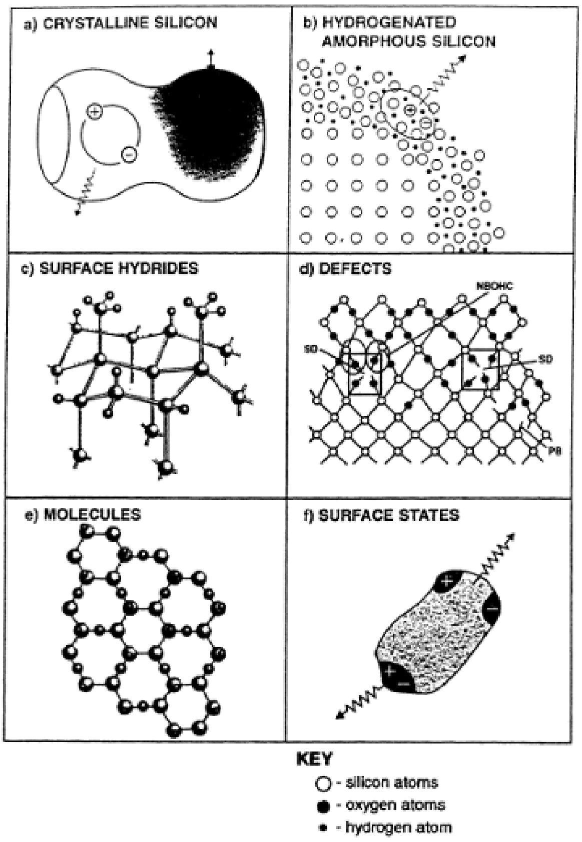

**Figure 9** Origin of luminescence from porous silicon [17].

(a) Quantum confinement effects result in an enlargement of the band gap, in a relaxation of the momentum-conserving rule, and in a size dependence of PL energy which naturally explains the efficient luminescence, the blueshift and the tunability of PL band in porous silicon. As illustrated in Figure 9a which is a section of an undulating crystalline quantum wire, a surface defect rends an undulation non-radiative, while an exciton localized in the neighboring undulation recombines radiatively. However, it is becoming increasingly clear that, even in the quantum confinement framework, the emission peak wavelength is not related only to size effects. Freshly etched and very high porosity samples which have not been exposed to the air have luminescence peak energies in the 3 eV range while as soon as they get into contact with air their luminescence peak moves to the usual 2 eV range. Thus, even though it is certain that quantum confinement plays a fundamental role in determining the abnormal properties of porous silicon, some complements to the pure quantum confinement model are needed. A change in the surface passivation, as well as dielectric effects, can produce wavelength shifts.

(b) It has been proposed that hydrogenated amorphous silicon formed during anodization possesses a PL band in the visible range. The disorder of the surface is responsible for radiative recombination. Nevertheless, TEM studies where sample damage has been minimized showed that there is very little amorphous silicon but the PL still exist.

(c) Silicon surface is passivated by six terminations. Radiative recombination may occur at the Si-H bonds. Against this model, after replacing the hydride coverage by a good quality oxide layer, the PL process still efficient.

(d) Partially oxidized silicon containing defects (defects in the silicon or silicon oxide that covers the surface) is proposed as the radiative centers. However, this model cannot explain tunability of the PL band because the emission from defects is insensitive to the size. Furthermore, in fresh porous silicon, the $SiO_2$ is not present.

(e) Siloxene molecule, an Si:H:O based polymer, supposedly created on the large inner PS surface, is proposed to acts as luminescence center. This model is rule out since porous silicon can still be luminescent above 800 $^{O}$C, while siloxene are totally decomposed.

(f) In surface states model, absorption occurs in quantum confined structures, but radiative recombination involves localized surface states; the external factors or the variation of the porous silicon chemistry is naturally accounted for by surface states changes. Either the electron, or the hole, or both or none can be localized. Hence, a hierarchy of transitions is possible which explains the various emission bands of porous silicon. Although there are some arguments against this model, it is still acceptable and frequently combined with the quantum confinement model.

## 3. Introduction to sol-gel chemistry

The sol-gel process, as the name implies, involves the evolution of inorganic networks through the transformation from “sol” to “gel”. The selected precursor materials are usually either inorganic salts or metal alkoxides. The precursors are generally soluble in organic solvent. A “sol” is defined as a colloid suspension with dispersed particles (1-1000 nm) derived from the hydrolyzed precursor in the liquid. By further hydrolysis and condensation reactions, the sol is then gelified to form a three-dimensional network trapping the solvent inside which is called a “gel”. These sol and gel formations can be carried out at low temperature (<100°C) and an oxide can be finally obtained after burning off the organic compounds by thermal treatment. A general sol-gel process is illustrated below [18]:

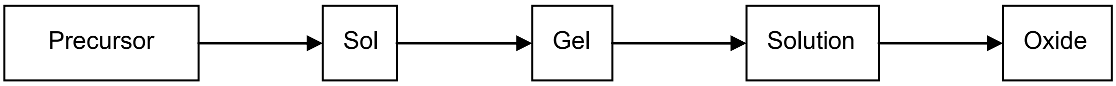

Generally, the sol-gel processing is based on a series of reactions which transform the system from “sol” to “gel”. Here we take the example of metal alkoxide [$M(OR)_n$] to interpret the fundamental chemistry of the sol-gel process [19-20]:

$$< \mathrm{Hydrolysis} >:$$

$$\mathrm{M-(OR)_n + xH_2O \rightarrow (OR)_{n-x} - M - (OH)_x + xROH} \quad (1)$$

$$< \mathrm{Condensation} >:$$

$$\mathrm{(OR)_{n-1} - M - (OH) + (OH) - M - (OR)_{n-1} \rightarrow (OR)_{n-1} - M - O - M - (OR)_{n-1} + H_2O} \quad (2)$$

$$\mathrm{(OR)_{n-1} - M - (OH) + (OR)_n - M \rightarrow (OR)_{n-1} - M - O - M - (OR)_{n-1} + ROH} \quad (3)$$

$$\mathrm{(OR)_{n-1} - M : (H_2O) + M - (OR)_n \rightarrow (OR)_{n-1} - M - OH - M - (OR)_{n-1} + ROH} \quad (4)$$

The hydrolysis involves the reaction of metal alkoxide with water Eq. (1). The “R” represents a proton or other organic groups and “ROH” is an alcohol. Eqs. (2–4) are the mechanisms of condensation and polymerization processes indicating that the water or alcohol molecules are liberated. These reactions can continue to build larger and larger units and finally form a polymeric structure. The reacted molecules may be in various forms from linear to 3-dimensional structures. The polymeric structures, such as dimers, chains and rings can be formed and ultimately lead to a

3-dimensional molecular network. As this molecular network is large enough to trap the solvent inside, the transformation from “sol” to “gel” is accomplished.

The structure of sol or gel is determined by the relative kinetics of the hydrolysis and condensation reactions. The final sol or gel structure plays a predominant role in determining properties of the resulting oxide products after thermal treatment. Many parameters are known to dominate the kinetics of gel formation and, as a consequence, strongly affect the properties of sol-gel derived materials. For sol-gel derived thin films fabrication, a good solution or its derived sol must be homogeneous, transparent and stable within the working period. This is absolutely necessary in order to obtain high quality of optical thin films especially for multi-stacked layers deposition. Some of the major parameters controlled are:

- The nature and reactivity of precursor materials are one of the most important parameters for the gel structures. The chemical reactivity depends mainly on the bonding behavior of the metal atom with organic groups, such as the electro-negativity and the coordination number of metal ions. Besides, it has been proved that the reactivity increases when the coordination number of metal decreases. Therefore, this coordination number is often adjusted in order to modify the reactivity of using precursor.

- The hydrolysis ratio that is the molar ratio of water to hydrolysable ligands [$H = H_2O/ (OR)$, i.e. the ratio (x/n) expressed in Eq. (1)]. When H is high, the hydrolysis reaction progresses quickly and tends to form a reticular network which is favorable for obtaining monoliths materials. Reversely, when H is small, the condensation is relatively predominant and leads to a polymeric structure (see Eq. 2 and 3) [21]. This parameter is often adapted for different destinations of material fabrications whether powders or films. In this work, the hydrolysis is carried out by atmospheric humidity control during film depositions.

- The chemical modification can effectively adjust the reactivity and hydrolysis rate of the sol-gel process, especially for high-sensitive precursors.

- The concentration of the solution is a crucial factor to the hydrolysis and condensation processes. When the concentration is lower, the reactive distance is relatively farther whereas the sol-gel process becomes strongly dependant on the system diffusion. Moreover, a low concentrated solution also allows to avoid the precipitation resulting from hydrolysis and also to reduce the viscosity. This is particularly an important parameter for the thin film preparation by “dip-coating” because the concentration of the solution dominates not only the gel structure but also the film density and thickness. In this work, various concentrations of yttrium alkoxides solutions are elaborated. The resulting film thickness and refractive index of the prepared thin films are shown to be strongly dependent.

- Except the parameters mentioned above, the temperature and pH value play also important roles in sol-gel process. The influence of pH is largely studied in the case of silicon alkoxide in which an acid catalyst is favorable for the hydrolysis reaction and a base catalyst is favorable for the condensation process. The temperature allows acceleration for all the reactions.

## ◈ Dip-coating process and apparatus

Some parameters are known to influence the deposited film properties during the dip-coating process. In this section, we will describe some of the important parameters controlled in this work.

### ➢ *Dip-coating process:*

The dip-coating method consists in soaking the substrate in the solution and withdrawing it at a constant speed. It has been observed that the soaking time may also affect the resulting film thickness [22]. A long soaking time increases the film thickness due to the adhesion of molecules from solution. The structures of films deposited by the dip-coating method depend on parameters related to the physical properties of the coating solution, such as structure of precursors, viscosity, surface tension and the relative rate of condensation and evaporation [23]. Before discussing the influence of solution properties to deposited films characteristics, the mechanism of sol-gel transition related to film formation during the dip-coating process must be understood. At the time of its withdrawal, the substrate supports a part of the solution in the form of a fluid film which is divided in two at the stagnation point “S” with the approach of the meniscus region as shown in Figure 10. The part located in the immediate neighborhood of the substrate accompanies with its rise, while the other remaining liquid falls back into the container. The intersection of the meniscus region with the surface separating the two parts defines a line of stagnation representing equilibrium between viscous stresses and gravity. The position of S thus determines the thickness of deposited film.

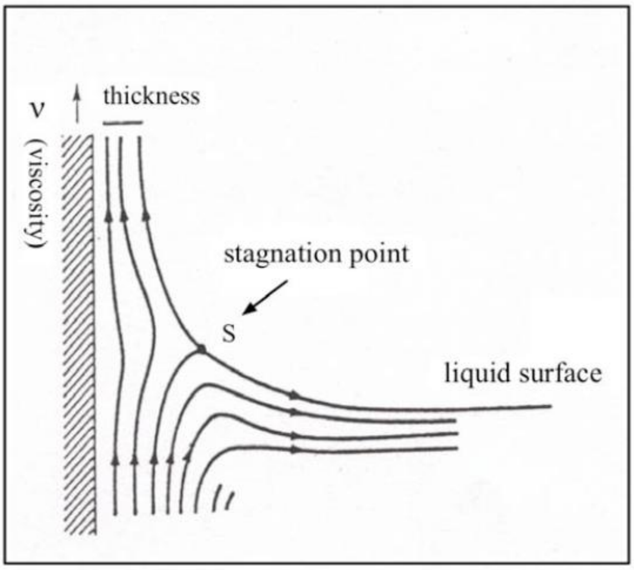

**Figure 10** Physical aspect of film deposition during dip-coating process.

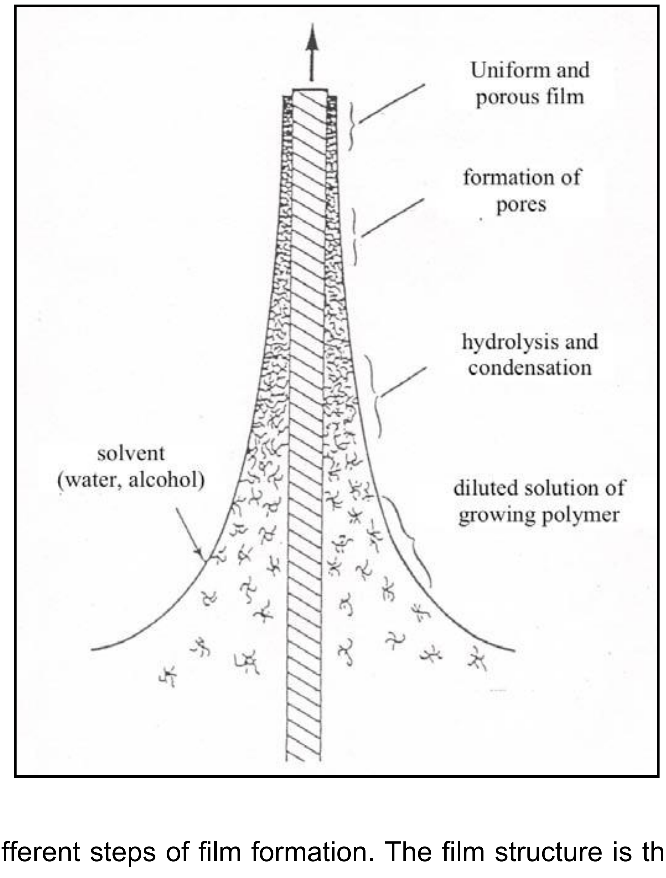

**Figure 11** The different steps of film formation. The film structure is the result of a compromise between drainage, evaporation of solvent and condensation.

As the substrate is withdrawn, the solution deposited onto the substrate undergoes a fast and spontaneous evolution as depicted in Figure 11. The precursor is quickly concentrated on the substrate by a draining force and evaporation of solvent. Simultaneously, the solution hydrolyzes and condenses by reacting with the atmospheric moisture and forms a polymeric structure. This drying process is an important step for thin film production. This step consists of the evaporation of the most volatile solvents by diffusion through the pores. During drying, the gel network can first collapse to accommodate the vacant spaces left by the solvent, preventing the creation of more open pores [24]. However, the simultaneous condensation and polymerization reactions strengthen the gel network during drying, and reduce the extent of shrinkage and the pore collapse [24]. Accordingly, the competition between evaporation and gelification allows us to control porosity by adjusting the kinetics of evaporation (solvent volatility, drying temperature, etc…) and condensation (precursor reactivity etc…).

### ➢ *Coating environment:*

To obtain thin films of extra-high optical quality, great attention must be paid at every step so as to reduce the number of defects, contaminations or inhomogeneities. As mentioned, the hydrolysis reaction of the deposited layer is carried out during the coating process. The atmospheric humidity control system is important and necessary. Since contaminants from the environment are always presented, an enclosed coating environment is absolutely necessary. A dry-box with an air flow control system can be used. The hydrolysis rate is adjusted by controlling the environmental humidity through injection of dry $N_2$ gas (containing less than 5ppm water) into the enclosure and monitoring by a hydrometer. In order to prevent disturbance from air-flow variations over the sample leading to thickness inhomogeneity, the air-flow is stopped when the desired humidity is attained to allow the drying process to complete in a stationary state. A Teflon container allows us to maintain the solution at a constant temperature and to reduce the possible vibration from environment disturbances. The solution container and motor must be isolated from any vibration to ensure that the coating sol remains completely undisturbed on the substrate. The withdrawing speed commonly used is in the range of 1 to 20 cm per minute.

Theoretically, the film thickness is given by the following relationship [25]:

$$\text{thickness} \propto \left[\frac{(\text{viscosity})(\text{withdrawing rate})}{(\text{sol density})}\right]^{1/2}$$

Of course this relationship is simplified because the viscosity and density of the solution may be varied during the coating operation due to solvent evaporation and condensation reactions, especially when the starting solution is very sensitive to humidity.

With careful control of operating parameters involving sol-gel and dip-coating processes, a wide range of film thickness from 4 nm [26] to 3000 nm [27] can be obtained. A uniform thickness of each coated layer is also successfully achieved [28].

### ➢ *Thermal treatments:*

For sol-gel derived materials, the thermal treatments mainly aim at carrying out the organic elimination in order to obtain a pure inorganic compound and furthermore to induce film crystallization. The film densification progresses at the same time. In this work, we use mainly quartz tubular furnace which is suitable to achieve the thermal treatment for thin films. This kind of furnace allows for atmosphere controlled thermal treatments, and the atmosphere is also easy to change. With this thermal system, the introduced gas is filtered by a molecular sieve to eliminate the possible contaminations existing in the air tube. This apparatus allows a thermal treatment in the range of 100°C to 1100°C, mainly limited by the softening point of the quartz tube. The as-coated layers can be annealed at various temperatures under either ambient air or other gas atmosphere depending on the aim of thermal treatment to activate film densification and structural evolution. In this work, the samples are mostly heat-treated under filtered $O_2$ atmosphere at each coating cycle in order to decompose the organic residuals. In some cases, the heat treatment is carried out under reduced gas such as $Ar/H_2$ to reduce the tetra-valence of terbium to tri-valence. The thermal treatment over 700°C is commonly done in ambient air for safety, because a possible violent chemical burn out might occur at high temperatures.

The high-K dielectric matrices ($SiO_2$, $ZrO_2$, $TiO_2$) were prepared by Sol-Gel technique. For $SiO_2$ matrix, tetraethoxysilane (TEOS) was dissolved in ethanol and then hydrochloric acid was added to generate hydrolysis reaction. The $ZrO_2$ matrix was made by dissolving zirconium n-propoxide [$Zr(OC_3H_7)_4$] in isopropanol and acetic acid was added to prevent moisture inducing precipitation of the sol and to maintain a stable sol. The fabrication of $TiO_2$ matrix is similar to $ZrO_2$ matrix; titanium isopropoxide [$Ti(OCH(CH_3)_2)_4$] was dissolved in isopropanol and acetic acid was also added in order to stabilize the sol. The procedures are summarized in Figure 12-14.

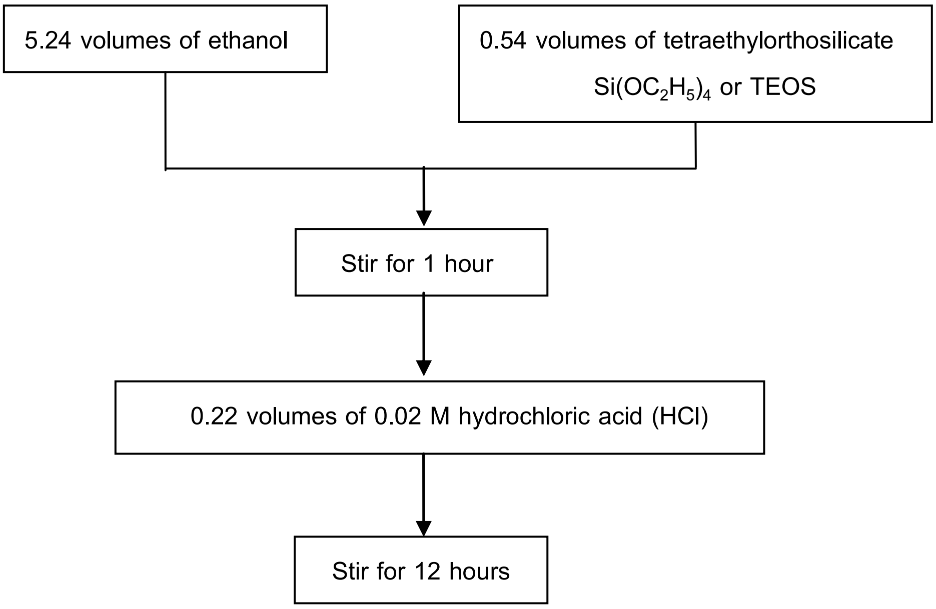

**Figure 12** Preparation of $SiO_2$ sol.

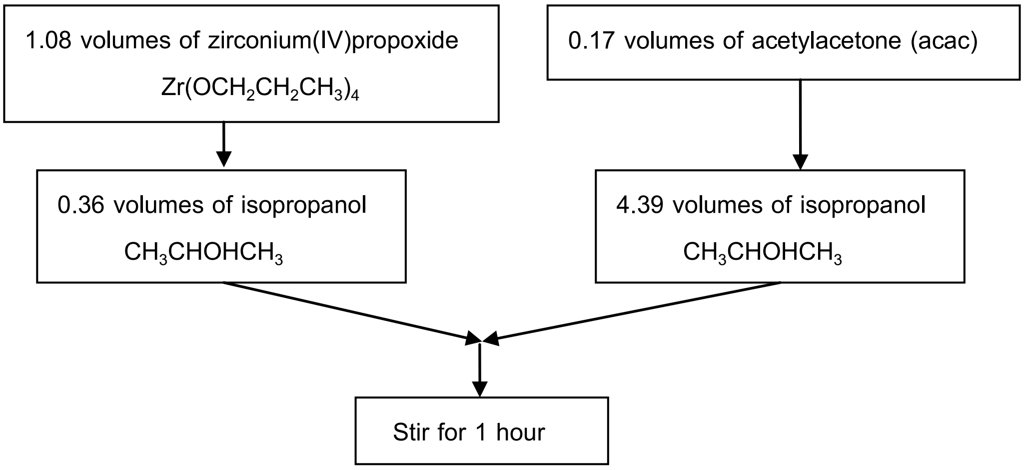

**Figure 13** Preparation of $ZrO_2$ sol.

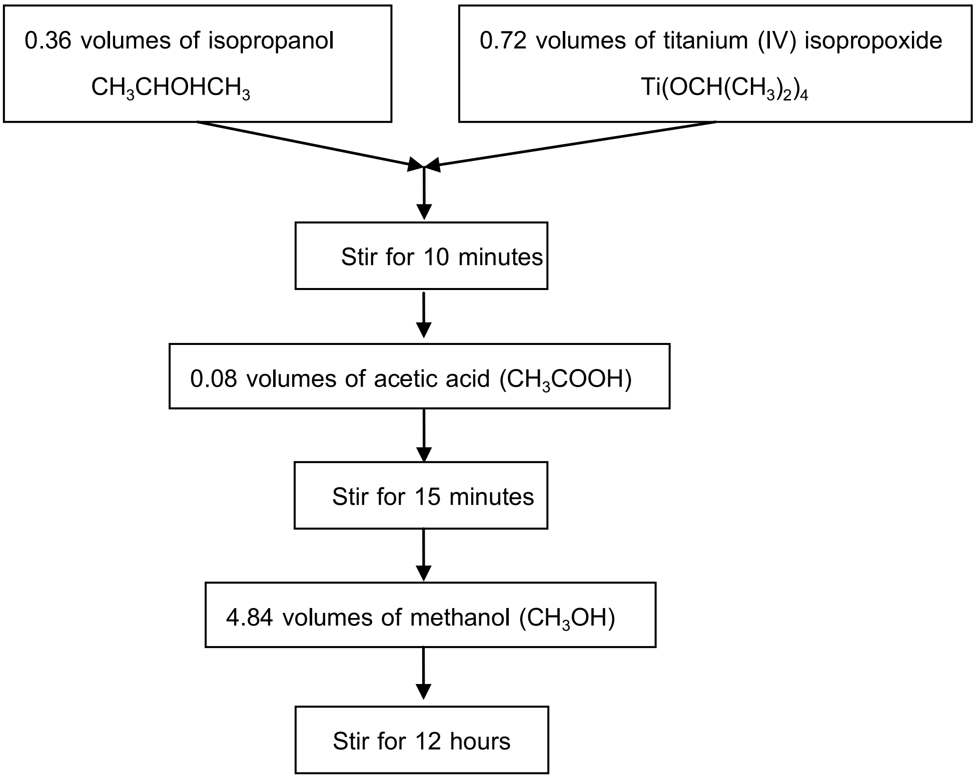

**Figure 14** Preparation of $TiO_2$ sol.

Silicon nanoparticles (Si-NPs) used herein were prepared by mechanical grinding of highly porous silicon (PS) layers which were fabricated by electrochemical etching of (100)-oriented silicon wafer slightly boron doped (resistivity of 3-10 Ω.cm). The electrolyte solution is a mixture of hydrofluoric acid and ethanol in a 1:1 volume ratio and the current density applied to the system is 54 mA/cm$^2$. After drying the etched silicon wafer in air, the PS nanostructures were harvested from the wafer and mechanical grinding was performed in a ball milling machine at rotation velocity of 300 rpm during 3 minutes to decompose the PS nanostructures down to homogenous nanopowder constituted by the separated elementary nanoparticles. Then, these PS powders were dispersed in pure ethanol.

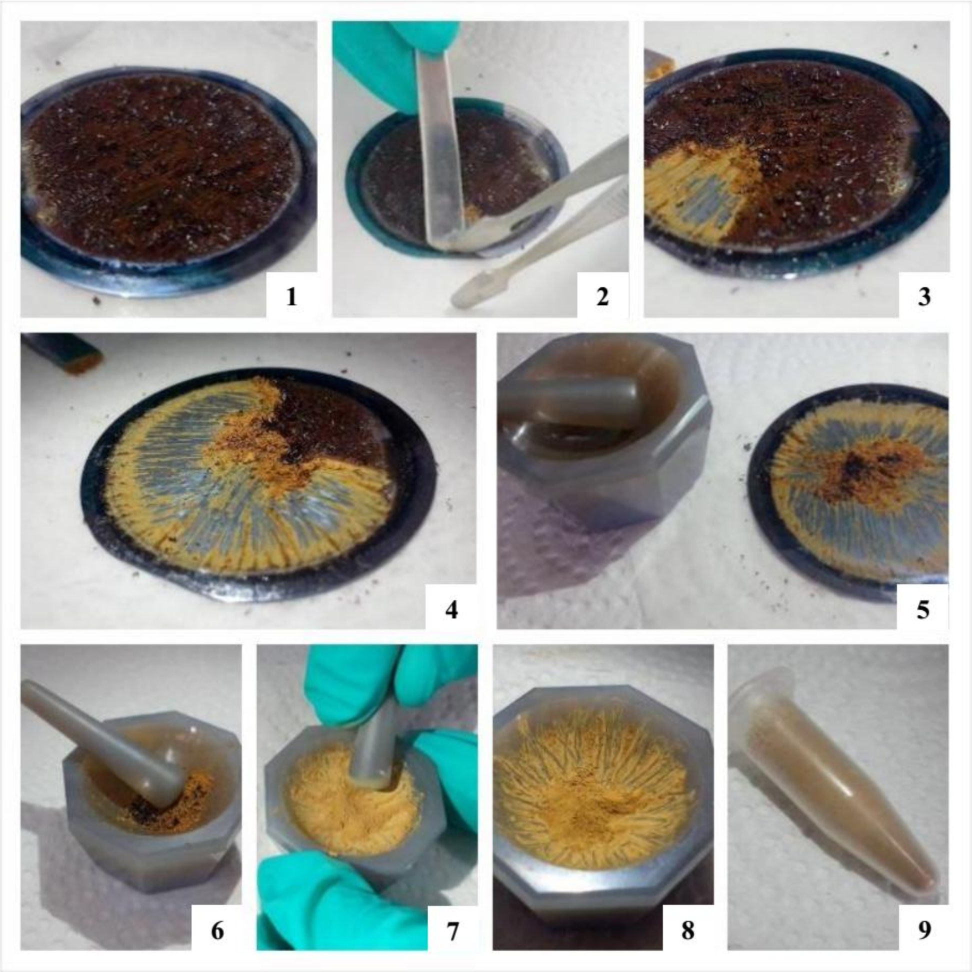

**Figure 15** Preparation of silicon nanoparticles (Si-NPs).

Next, these colloidal solutions were mixed with the Sol-Gel solutions at the concentrations of 1, 3 and 5 g/L. The mixtures were dried in Pyrex plates at 90°C during 3 days and annealed at 300°C for 1 hour. After annealing, the solvents were eliminated and the solid oxide matrices with the Si-NPs trapped inside were formed.

To fabricate thin oxide films containing the Si-NPs, the colloidal suspension of Si-NPs was let to sediment for 3 days. Then, the supernatant liquid ethanol containing the small grain Si-NPs was harvested and mixed with the Sol-Gel solutions. Using the dip-coating method with a withdrawal speed of 7 cm/min, thin films were deposited onto the substrates. Then, the films were annealed for 5 minutes at 100°C and 15 minutes at 300°C between each coating under $O_2$ flow to support organic burnout of the films. The dipping was repeated until obtaining the film thickness about 300 nm. Finally, the films were annealed again at the following temperatures: 400°C, 500°C, 600°C, 800°C and 1000°C.

A number of characteristics of Si-NPs in different dielectrics were done by using Raman-scattering, Photoluminescence spectroscopy and Transmission electron microscopy. Raman-scattering measurements were operated at room temperature in a backscattering configuration using 488 nm Argon laser light and a Dilor XY monochromator coupled with a CCD detector. The room temperature PL measurements were also carried out using the 458 nm Argon laser light of 35 mW power as excitation source. The PL signal is dispersed by a Jobin-Yvon type HRS-2 spectrometer and detected using a PM Hamamatsu (H5701-50). Finally, all spectra were corrected for the spectral response of the full optical system. TEM measurements were performed by using a high resolution analytical microscope TOPCON EM-002B operating at 120 kV and 200 kV.

Raman measurements were carried out for Si-NPs incorporated in different dielectric matrices ($SiO_2$, $ZrO_2$ and $TiO_2$) and also for Si-NPs without matrix. Note that, in our case, Raman responses of the matrices could overlap with those of Si-NPs; therefore, in order to clearly observe the peak of Si-NPs, its concentration must be sufficiently high. Hence, in this study, the initial concentrations of NPs selected are 1, 3 and 5 g/L, respectively. Raman spectra of Si-NPs embedded in $SiO_2$, $ZrO_2$ and $TiO_2$ matrices at different concentrations are shown in Figures 16 -18.

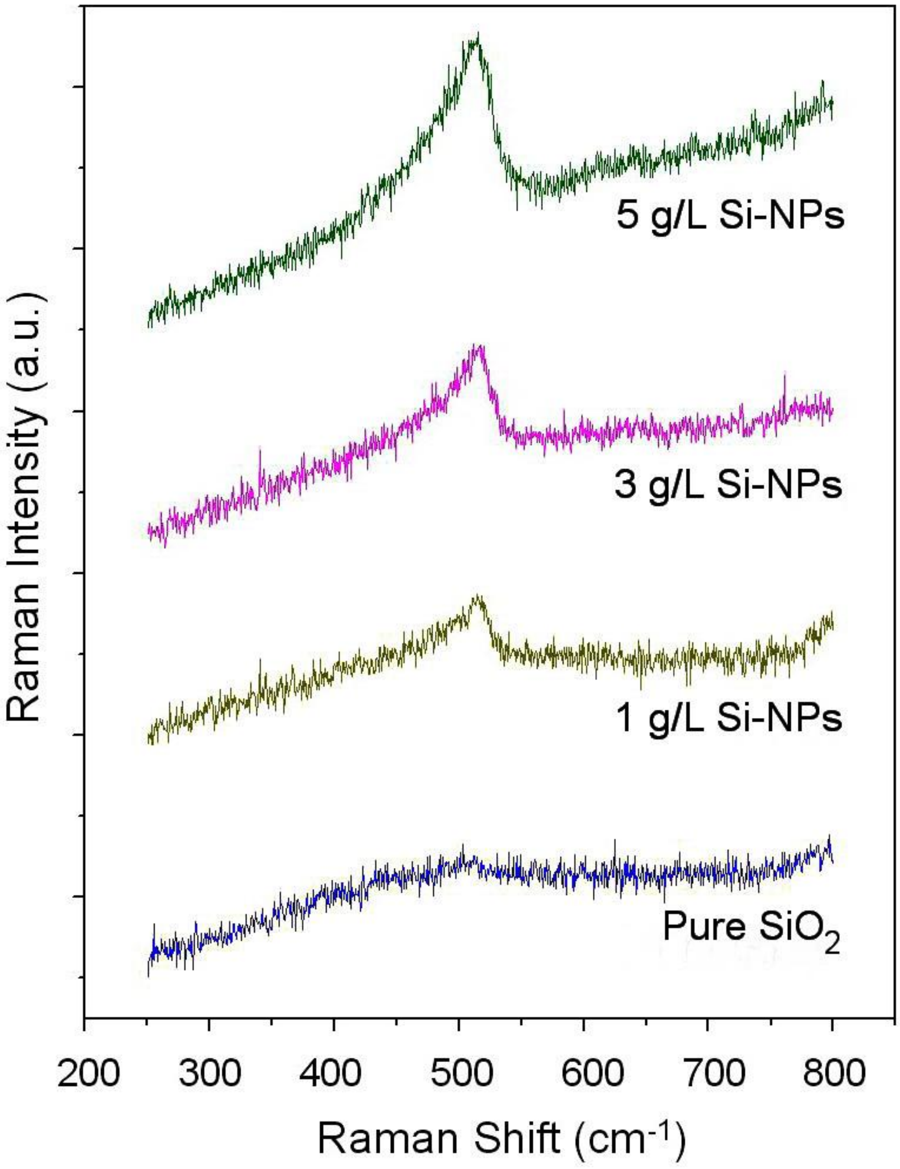

**Figure 16** Raman spectra of Si-NPs incorporated into $SiO_2$ matrix at different concentrations.

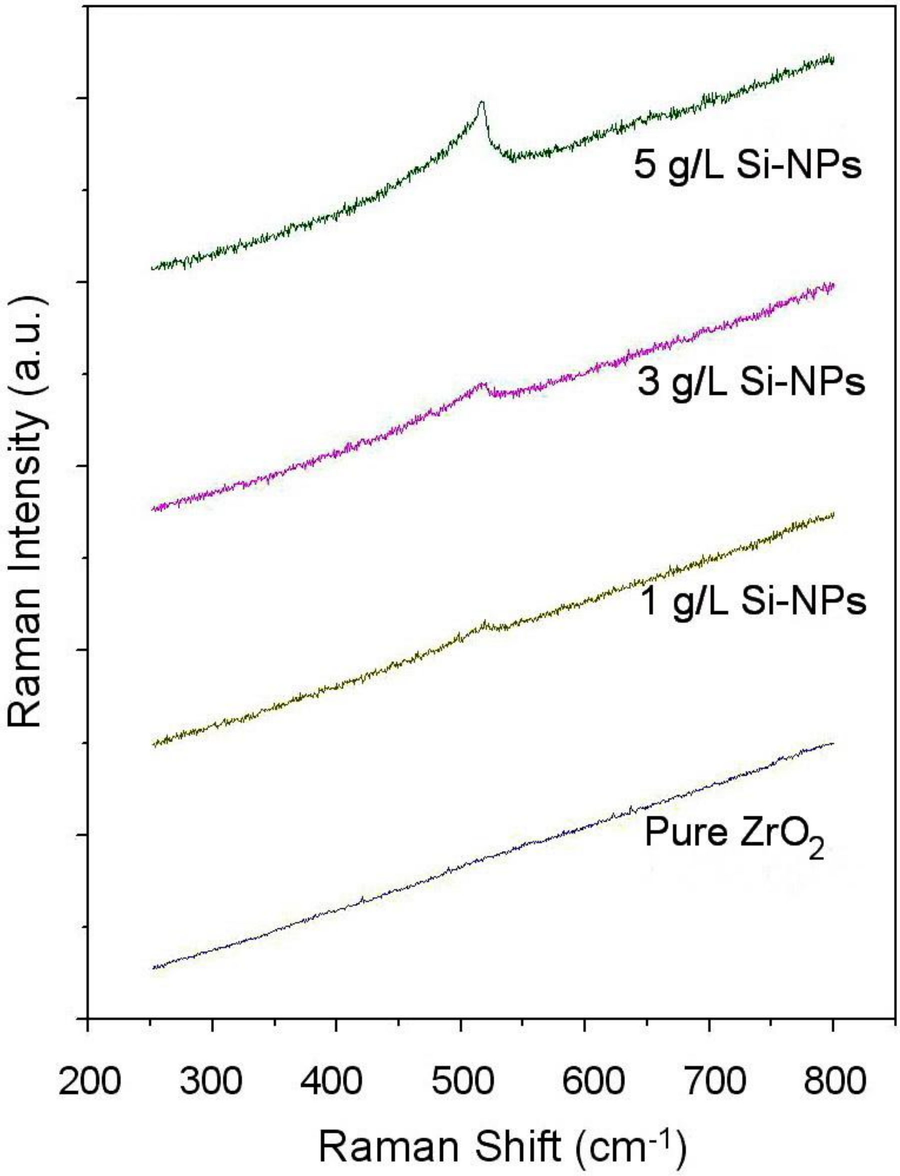

**Figure 17** Raman spectra of Si-NPs incorporated into $ZrO_2$ matrix at different concentrations.

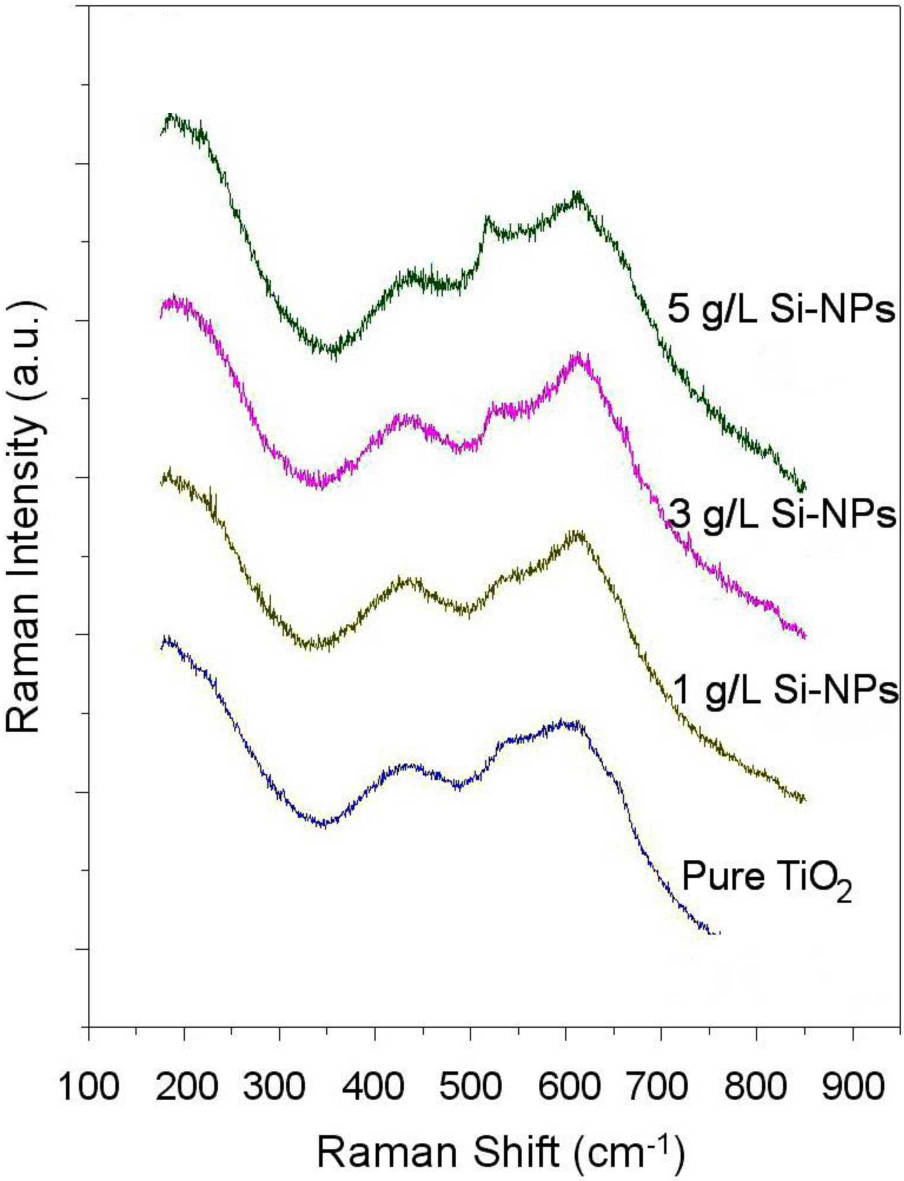

**Figure 18** Raman spectra of Si-NPs incorporated into $TiO_2$ matrix at different concentrations.

For pure matrices, it was found that all matrices were in amorphous phase and when Si-NPs were incorporated in the matrix, a peak near 517 cm$^{-1}$ is observed. Furthermore, the intensity of this peak increases with the concentration of Si-NPs. To obtain only the peak of Si-NPs, the total responses are subtracted by the Raman spectra of pure matrix. However, the subtraction could not be done for $TiO_2$ matrix due to the overlapping of the Si-NPs peak with that of the $TiO_2$ matrix. The resulted spectra after subtraction for $SiO_2$ and $ZrO_2$ matrices are illustrated in Figures 19 and 20, and the Raman spectra of free silicon nanoparticles (non-incorporated into any matrices) are also shown in the same figures to be compared. Note that all spectra were normalized.

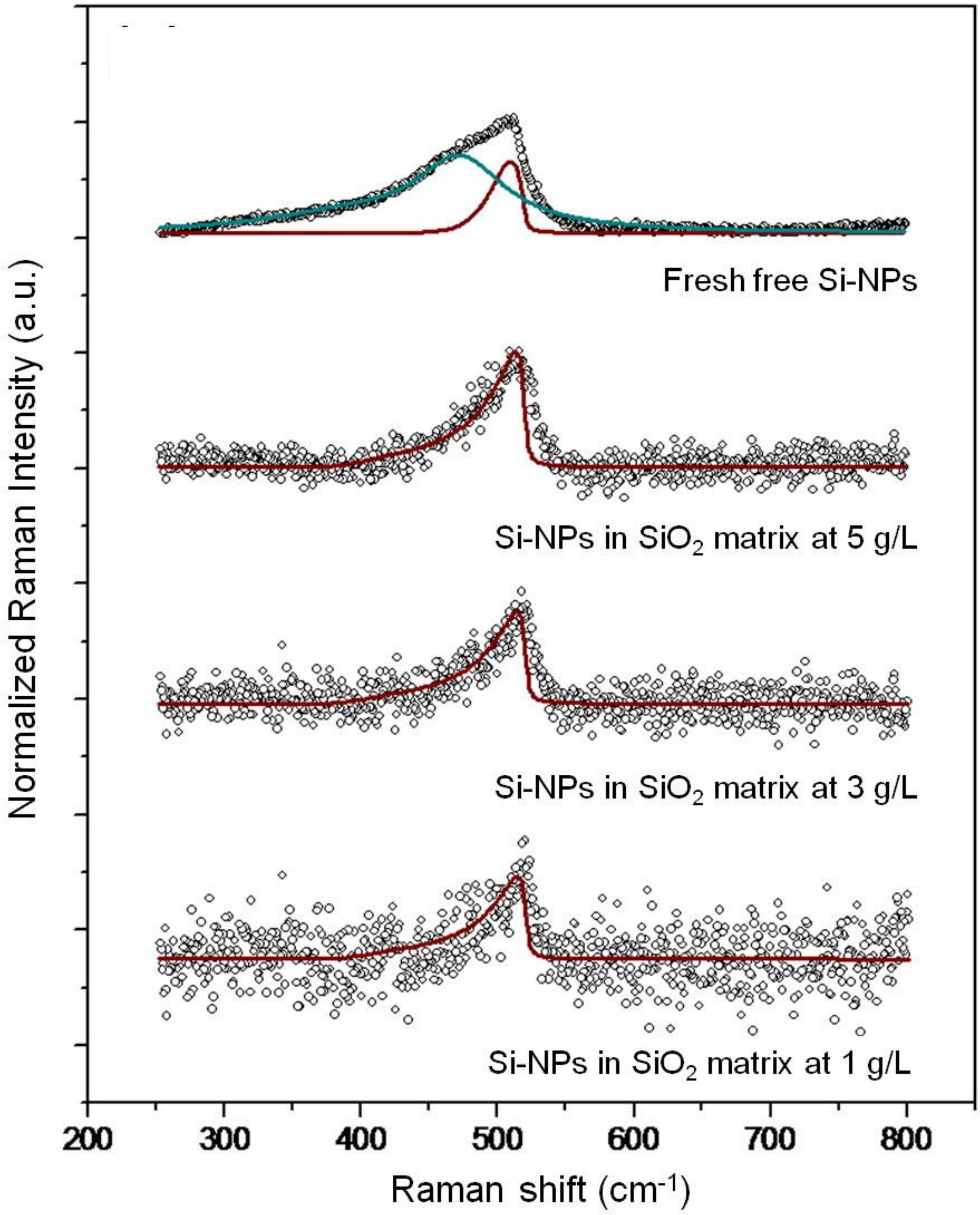

**Figure 19** Raman spectra of Si-NPs after subtraction of $SiO_2$ matrix.

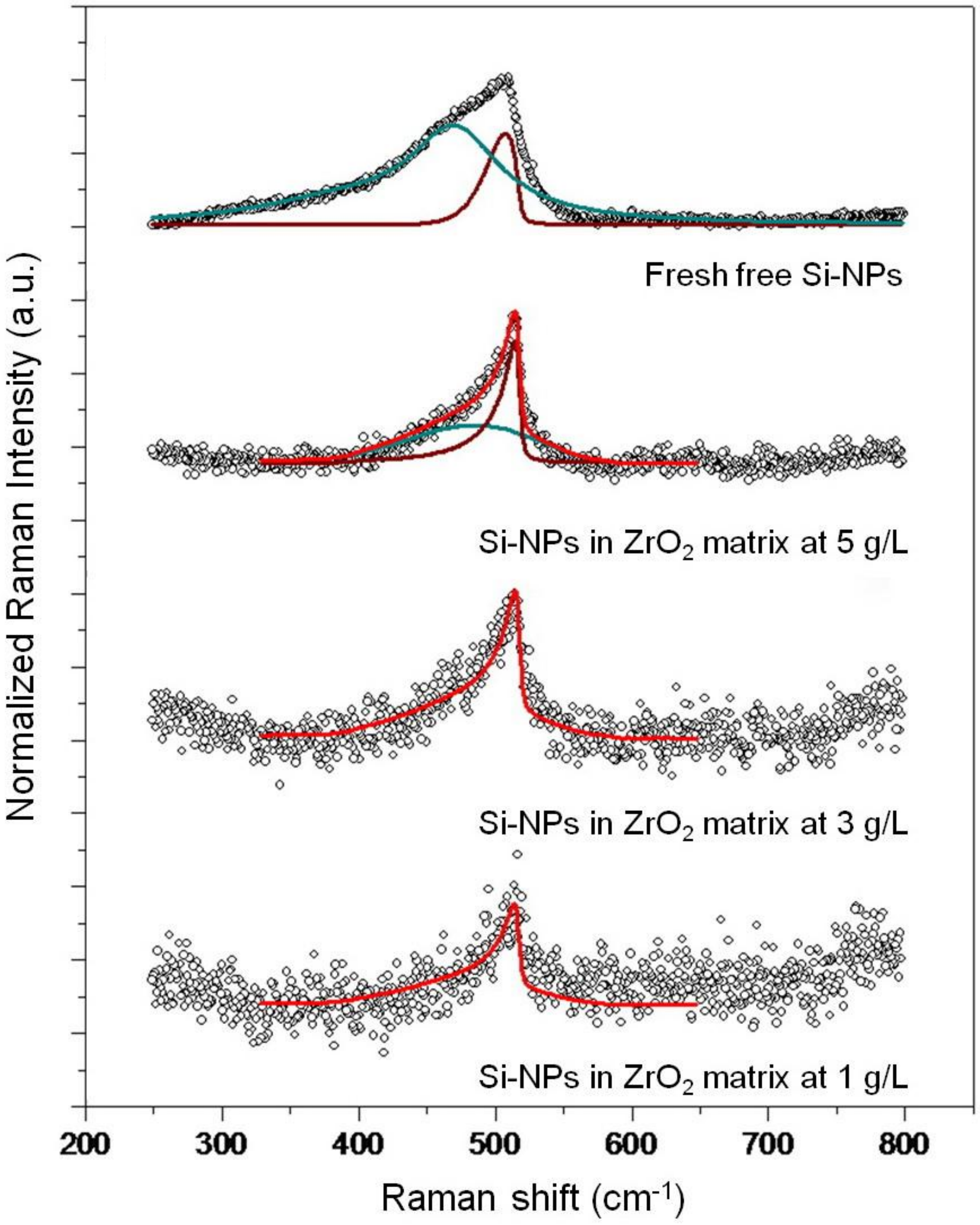

**Figure 20** Raman spectra of Si-NPs after subtraction of $ZrO_2$ matrix.

In case of free Si-NPs, we observe an important shift of the Raman peak toward higher vibration energy (509 $\mathrm{cm}^{-1}$) comparing to monocrystalline silicon (521 $\mathrm{cm}^{-1}$). This peak can also be decomposed into two independent peaks: the first asymmetric and relatively fine peak is centered at 508.8 $\mathrm{cm}^{-1}$ and the second Gaussian-like large band is situated at 470 $\mathrm{cm}^{-1}$. According to widely accepted explanation [29], these contributions correspond to crystalline core and to amorphous phase of the near-surface region of the Si-NPs, respectively. The fine peak related to the crystalline phase was determined by using the quantum confinement model of Campbell and Fauchet [30] combined to Gaussian distribution of the nanoparticle dimensions [31]. This model allows estimation of a mean dimension value of the NPs with its standard deviation. In our case, the nanoparticle dimensions were estimated to 3.6 ± 0.5 nm. It is also important to note that for the free Si-NPs, the Raman peak intensity of amorphous phase is comparable to that of quantum confinement model.

In order to apply the quantum confinement model to the Si-NPs incorporated in the matrix, the highest concentration of 5 g/L was chosen for the model owing to its lowest noise and the other concentrations were fitted by using a multiplying factor. For Si-NPs in $SiO_2$ matrix, the quantum confinement model fits suitably with the experimental result, contrarily to the Si-NPs in $ZrO_2$ matrix. Since the amorphous phase appears in case of $ZrO_2$ matrix, the model has to be fitted in the same way as for the free Si-NPs.

It was found that for these two matrices, the Raman peak of Si-NPs ($\approx$ 517 $\mathrm{cm}^{-1}$) shifts toward higher vibration energies comparing to the Raman peak of monocrystalline silicon. (This shift is also observed in $TiO_2$ matrix doped at 5 g/L of concentration.) Although the peak position is higher than that of free-Si NPs (509 $\mathrm{cm}^{-1}$), it remains lower than that of monocrystalline silicon (521 $\mathrm{cm}^{-1}$). In fact, this significant blueshift of the Raman peak (on about 8-9 $\mathrm{cm}^{-1}$) can be explained by mechanical stresses undergone by the NPs from the matrix side [32]. By taking into account hydrostatic model describing the exercised stresses [33], which is relatively convenient for the incorporated zero-dimensional NPs, we have found that this important compressive stress has the value about 1.9 GPa.

We also noted that the full width at half maximum (FWHM) of the peak corresponding to the Si-NPs incorporated in the matrices is much narrower than that of the free Si-NPs. The following explanation can be as follows: The compressive stress leads to partial or even complete blocking of the superficial vibrations of the nanoparticles which is situated in direct close contact with the compressing matrix. This stress impact can even favor the arrangement of the superficial Si-Si bonds leading to their structural ordering; therefore, make the recorded Raman peaks narrower.

Moreover, we found that the proportion of nanoparticles' amorphous phase decreases when the NPs were encapsulated in the matrix. This phenomenon is more significant in case of $SiO_2$ matrix because the quantum confinement model fits well with the experimental spectrum without appearance of amorphous phase. In fact, this effect may be related to oxidation of NPs during sample preparation. As the amorphous phase is in direct contact with the matrix, it is therefore more susceptible to be oxidized and make the diminution of the Raman responses of amorphous phase. However, for $ZrO_2$ matrix, we can observe the presence of amorphous phase even though it was very low. This happens due to the fact that, the kinetic of $SiO_2$ formation by sol-gel method is generally slow; thus, in order to accelerate the gelification of $SiO_2$ sol, a quantity of acid must be added to the solution and it requires 3 days for the gel to be solidified and dried at room temperature. The NPs are thus in contact with the sol-gel solution (water and other solvents), and during this period, the oxidation could be occurred. This phenomenon is less influential for $ZrO_2$ matrix because its sol-gel process is faster.

The room temperature PL measurements were achieved using 488 nm (2.54 eV) of excitation. This wavelength was selected with 2 criteria: first, it must not be absorbed by the matrices; the energy is smaller than the energy gap of the considered matrices ($SiO_2$: 9 eV, $ZrO_2$: 5.8 eV, $TiO_2$: 3.5 eV), and second, it must be sufficient to generate electron-hole pairs in silicon, despite the increase of transition energy when its size diminishes. The PL spectra of the free Si-NPs and the Si-NPs encapsulated into the matrices are shown in Figures 21 and 22.

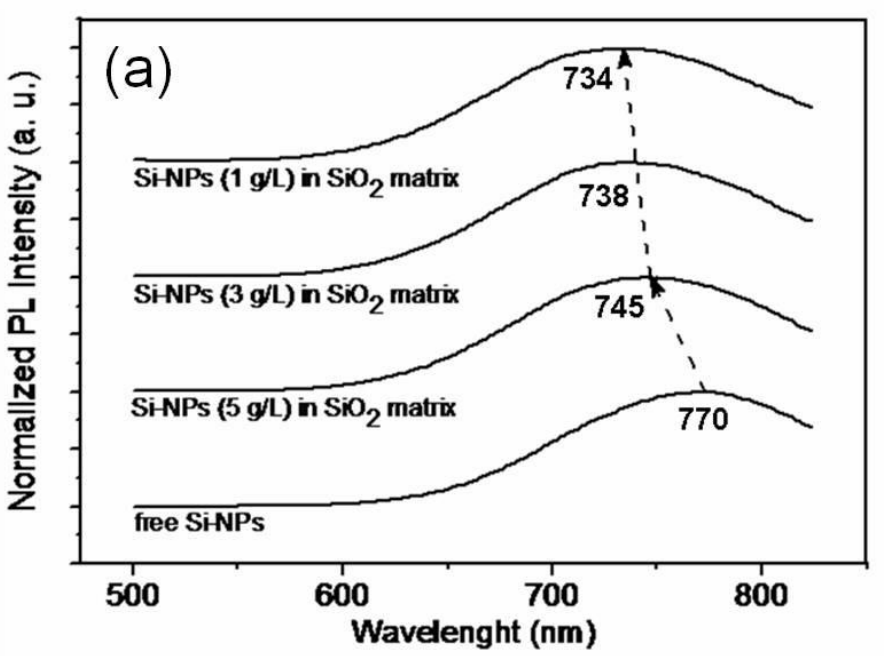

**Figure 21** Normalized PL spectra of Si-NPs incorporated into $SiO_2$ matrix at different concentrations compared to the normalized PL spectrum of free Si-NPs.

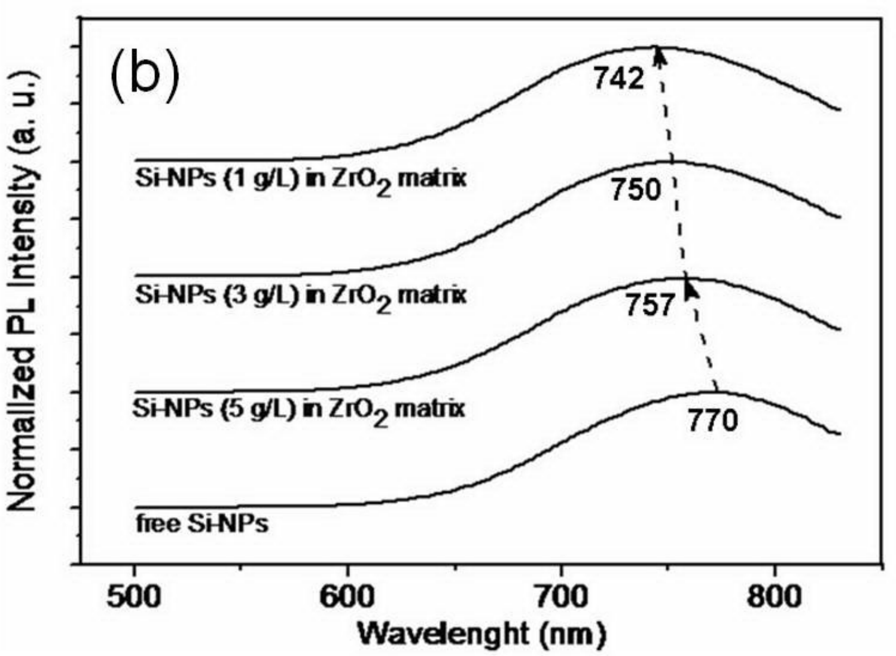

**Figure 22** Normalized PL spectra of Si-NPs incorporated into $ZrO_2$ matrix at different concentrations compared to the normalized PL spectrum of free Si-NPs.

Considering the mean dimension of the free Si-NPs (3.6 nm) estimated from the Raman studies previously discussed, it was found that the PL band position of the free Si-NPs (770 nm) was in good agreement with the quantum confinement model describing PL properties of nanocrystalline silicon [34].

Nevertheless, when the Si-NPs were encapsulated in the matrices, two phenomena were observed:

- The PL band of the Si-NPs encapsulated in the matrices shifts toward higher energy «blueshift» in comparison to the PL spectrum of the free Si-NPs. This phenomenon could be related to the oxidation of Si-NPs inside the matrix. The NPs become thus smaller and exhibit the luminescence at higher energies. In addition, we notice that the maximum of PL bands of the Si-NPs in $SiO_2$ matrix shifts more than that in $ZrO_2$ matrix. This happens because the gelification kinetic of $SiO_2$ is slower than that of $ZrO_2$ as discussed in Raman measurements.
- The PL band of the Si-NPs slightly shifts toward lower energy «redshift» when its concentration in the matrix increases. In fact, this redshift corresponds to coupling between the nanoparticles; for higher concentrations of NPs, the interconnection number increases (i.e. mean distance between the NPs decreases) and, consequently, the band gap of the aggregates formed by the interconnected NPs becomes narrower.

In case of the Si-NPs incorporated into $TiO_2$ matrix, no PL signal from the Si-NPs was detected despite the presence of Si-NPs peak in Raman studies which is shown in Figure 1(c). This can be understood by taking into account the fact that the band gap of the $TiO_2$ matrix (3.5 eV) is too closed to the band gap value of Si-NPs (1.6–1.8 eV). In such matrix the quantum confinement of photogenerated charge carriers in Si-NPs is not satisfied because the electrons can move from conduction band of the NPs to that of the $TiO_2$ matrix (CB offset: 0 eV) [35].

The incorporation of the NPs into the matrices was also observed by Transmission Electron Microscopy. Because of the low contrast between the matrices and Si-NPs, the latter cannot be distinguished from the matrix background at low spatial resolution. However, lattice fringes of Si-NP can be clearly seen on the amorphous background of the $ZrO_2$ and $TiO_2$ matrices in highly resolved TEM images. The TEM images of Si-NPs before and after incorporation into the matrices are shown in Figure 23 and Figure 24, respectively.

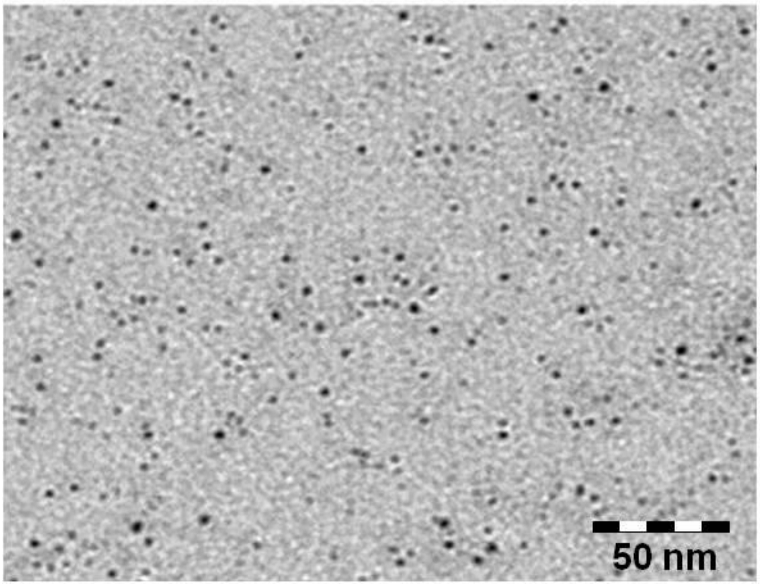

**Figure 23** TEM image of free Si-NPs dispersed in ethanol and filtered with 200 nm membrane filter.

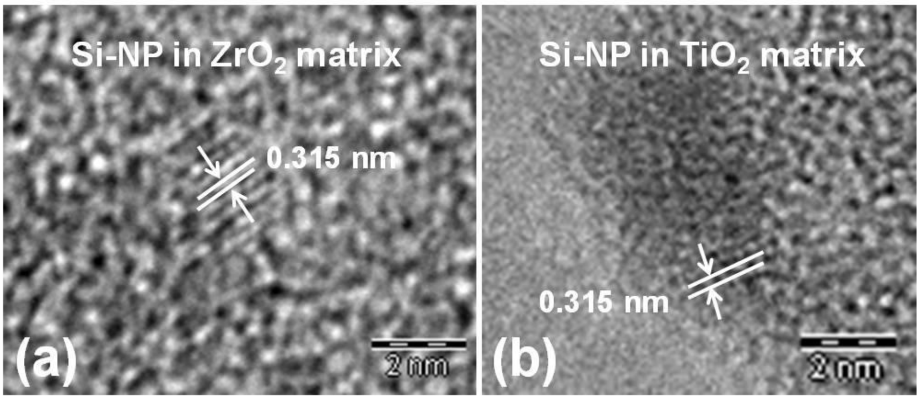

**Figure 24** TEM images of the Si-NP encapsulated in $ZrO_2$ matrix (a) and $TiO_2$ matrix (b).

The PL spectra of the Si-NPs in $SiO_2$ thin film and in $ZrO_2$ thin film are depicted respectively in Figure 25 and 26. In case of thin films annealed at 300°C, the PL peak position of the Si-NPs encapsulated in $SiO_2$ matrix and in $ZrO_2$ matrix are both situated around 732 nm of wavelength. Taking into account the quantum confinement of photogenerated charge carriers in the NPs, which generally depends on the size of NPs and on the surrounding matrix, it was found that the NPs have the same size distribution in both matrices at this annealing temperature. However, when the samples were annealed at higher temperatures, we noticed that the Si-NPs in $SiO_2$ matrix have more thermodynamic stability than in $ZrO_2$ matrix. As illustrated in Figure 25, when the annealing temperatures increase, the PL peak positions of the NPs in $SiO_2$ matrix is almost unchanged whereas the PL peak intensities decrease. In fact, the decrease of PL intensity in $SiO_2$ matrix can be provoked by the loss of the Si-H bonds situated on the surface of the NPs which occurs after 600°C annealing [36]. Furthermore, size diminution of the NPs induced by oxidation can be observed in PL spectra of NPs inside the $ZrO_2$ matrix [37] (Figure 26). After 400°C of annealing, the NPs become smaller, and we can observe the peak of small NPs situated around 558 nm and the peak of large NPs situated at 735 nm. At 500°C, the small NPs become predominant thus the peak of large NPs cannot be distinguished. Finally, when the annealing temperature reaches 1000°C we can observe again the peak of large NPs but it provides very low intensity. This experiment shows thus that thermodynamic stability of Si-NPs in $SiO_2$ matrix is higher than in $ZrO_2$ matrix.

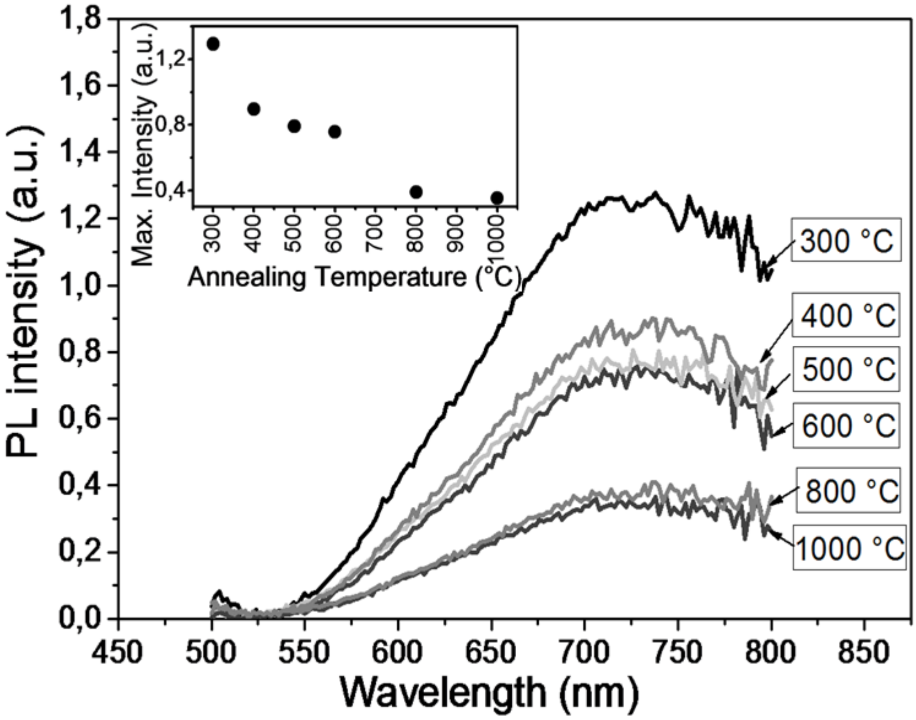

**Figure 25** PL spectra of the Si-NPs encapsulated into $SiO_2$ thin film annealed at various temperatures 300°C, 400°C, 500°C, 600°C, 800°C and 1000°C. Inset: Maximum PL intensity of the sample in function of the annealing temperatures.

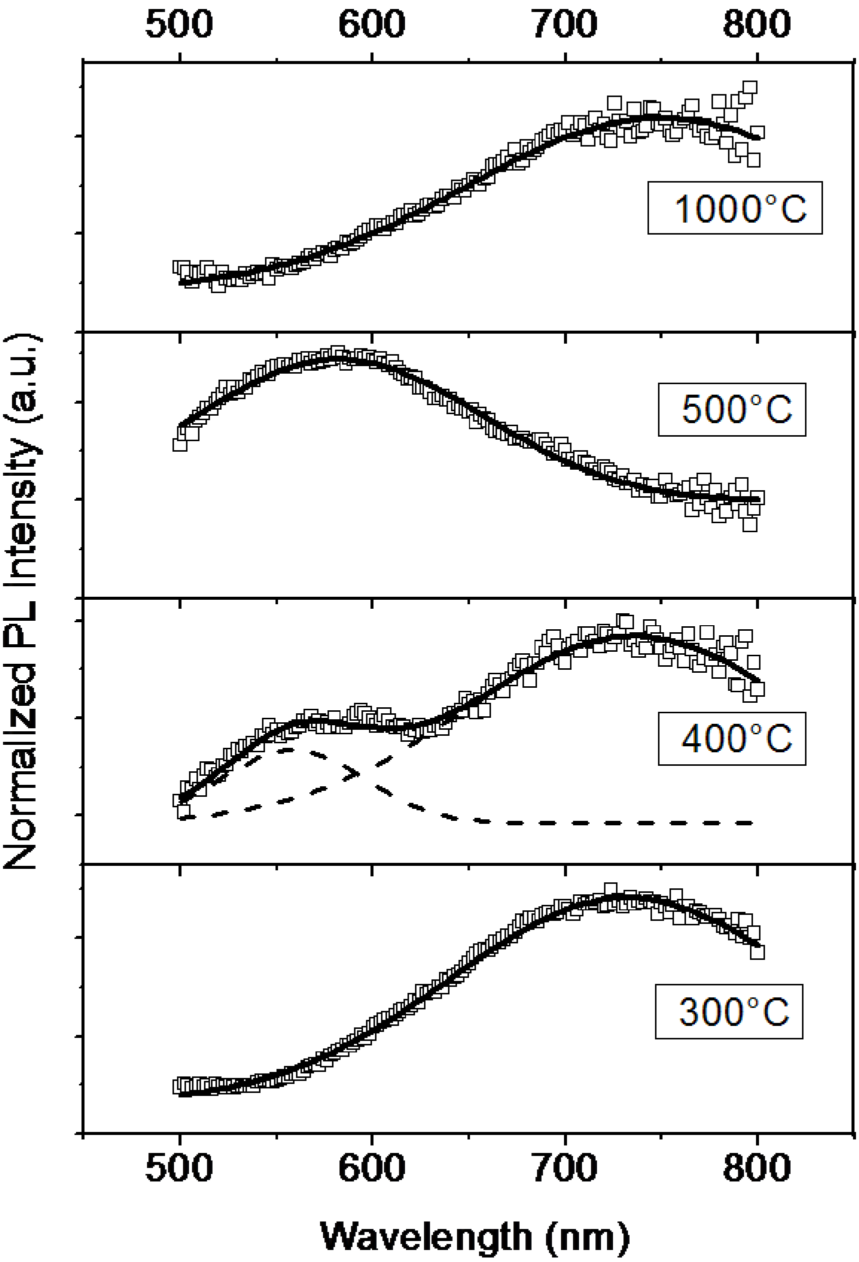

**Figure 26** Normalized PL spectra of the Si-NPs encapsulated into $ZrO_2$ thin film annealed at different temperatures 300°C, 400°C, 500°C and 1000°C.

# Conclusion

In this work, incorporation of Si-NPs in different dielectric matrices was carried out by using the Sol-Gel technique. The influences of host matrices on structural and photoluminescent properties of the Si-NPs were examined, in particular, the significant compressive stress which is responsible for structural modification of the NPs. The NPs encapsulated inside the $SiO_2$ and $ZrO_2$ matrices exhibit bright photoluminescence at room temperature due to efficient quantum confinement of the photogenerated carriers in the nanoscale Si particles contrarily to the NPs encapsulated in the $TiO_2$ matrix. The PL peak position depends on average dimension and concentration of NPs. The overall results satisfactorily confirm the feasibility to apply the Sol-Gel technique to the fabrication of nanoelectronic devices.

# References

---

[1] V. Kumar, *Nanosilicon*, Elsevier, Chennai, India, (2007).

[2] D. Nesheva, C. Raptis, A. Perakis, I. Bineva, Z. Aneva, Z. Levi, S. Alexandrova and H. Hofmeister, J. Appl. Phys. 92, 4678 (2002).

[3] G. Santana, B. M. Monroy, A. Ortiz, L. Huerta, J. C. Alonso, J. Fandiño, J. Aguilar-Hernández, E. Hoyos, F. C.- Gandarilla and G. C.- Puentes, Appl. Phys. Lett. 88, 041916 (2006).

[4] G. H. Li, K. Ding, Y. Chen, H. X. Han and Z. P. Wang, J. Appl. Phys. 88, 1439 (2000).

[5] P. R. Watekar , S. Ju and W.-T. Ha, Curr. Appl. Phys. 9, S182 (2009).

[6] H. R. Huff and D.C. Gillmer, *High Dielectric Constant Materials: VLSI MOSFET Applications*, Springer, Berlin (2004).

[7] H. Shimizu and T. Nishide, *Advances in Crystallization Processes*, InTech, (2012).

[8] V. Svrcek, A. Slaoui and J.-C. Muller, J. Appl. Phys. 95, 3158 (2004).

[9] Y. Posada, L. S. Miguel, L. F. Fonseca, O. Resto, S. Z. Weisz, C.-H. Kim and J. Shinar, J. Appl. Phys. 96, 2240 (2004).

[10] J. Valenta, P. Janda, K. Dohnalova, D. Niznansky, F. Vacha, J. Linnros, Opt. Mater. 27, 1046 (2005).

[11] K. Luterova, K. Dohnalova, F. Trojanek, K. Neudert, P. Gilliot, B. Honerlage, P. Maly, I. Pelant, J.Non-Cryst. Sol. 352, 3041 (2006).

[12] O. Bisi, S. Ossicini and L. Pavesi, Surf. Sci. Rep. 38, (2000).

[13] V. Lehmann and U. Gösele, J. Ind. Eng. Chem. 58, 856 (1991).

[14] R. L. Smith and S. D. Collins, J. Appl. Phys. 71, R1 (1992).

[15] M. Wesolowski, Phys. Rev. B 66, 205207 (2002).

[16] F. Zhou and Y. M. Huang, Appl. Surf. Sci. 253, 4507 (2007).

[17] A. G. Cullis, L. T. Canham and P. D. J. Calcott, J. Appl. Phys. 82, 909 (1997).

[18] C. J. Brinker and G. W. Scherrer, Sol-gel science: the physics and chemistry of sol-gel processing, Acadamic Press, New York, 1990

[19] D. C. Bradly, R. C. Mehrotra, D. P. Gaur, Metal alkoxides, Academic Press, London, 1978

[20] R. C. Mehrotra, J. Non-Cryst. Solids 100, 1 (1988).

[21] L. G. Pfalzgraf, “Alkoxide as molecular precursors for oxide based inorganic materials: opportunities for new materials”, New Journ. Chem., 11 (1987) 665

[22] S. Parola, M. Verdenelli, C. Sigala, J. P. Scharff, K. Velez, C. Veytizou, J. F. Quinson, J. Sol-Gel Sci. Tech. 26, 803 (2003).

[23] C. J. Brinker, G. C. Frye, A. J. Hurd and C. S. Ashley, Thin Solid Films 201, 97 (1991).

[24] C. J. Brinker, R. Sehgal, S. L. Hietala, R. Deshpande, D. M. Smith, D. Loy and C. S. Ashley, J. Membrane. Sci. 94, 85 (1994).

[25] I. M. Thomas, “Optical coating fabrication”, Sol-gel Optics: Processing and applications, L. C. Klein Ed., Kluwer Academic Publications, Massachusettes, (1994).

[26] A. Brioude, F. Lequevre, J. Mugnier, J. C. Plenet, J. Appl. Phys. 88, 6187 (2000).

[27] C. Le Luyer, L. Lou, C. Bovier, J. C. Plenet, J. G. Dumas, J. Mugnier, Opt. Mat. 18, 211 (2001)

[28] S. Rabaste, J. Bellessa, A. Briode, C. Bovier, J. C. Plenet, R. Brenier, O. Marty, J. Mugnier, Thin Solid Films 416, 242 (2002).

[29] A. Singha, P. Dhar and A. Roy, Am. J. Phys. 73, 224 (2005).

[30] I. H. Campbell and P. M. Fauchet, Solid State Commun. 58, 739 (1986).

[31] M. N. Islam and S. Kumar, Appl. Phys. Lett. 78, 715 (2001).

[32] I. D. Sharp, D. O. Yi, Q. Xu, C. Y. Liao, J. W. Beeman, Z. Liliental-Weber, K. M. Yu, D. N. Zakharov, J. W. A. III, D. C. Chrzan and E. E. Haller, Appl. Phys. Lett. 86, 063107 (2005).

[33] F. Cerdeira, C. J. Buchenauer, F. H. Pollak and M. Cardona, Phys. Rev. B 5, 580 (1972).

[34] P. M. Fauchet and J. V. Behren, Phys. Stat. Sol. 204, R7 (1997).

[35] J. Robertson, Rep. Prog. Phys. 69, 327 (2006).

[36] V. Lysenko, F. Bidault, S. Alekseev, V. Zaitsev, D. Barbier, C. Turpin, F. Geobaldo, P. Rivolo, and E. Garrone, J. Phys. Chem. 109, 19711 (2005).

[37] M. Copel, M. Gribelyuk, and E. Gusev, Appl. Phys. Lett. 76, 436 (2000).